AIP Journal of Applied Physics

Microannular electro-osmotic flow with the axisymmetric lattice Boltzmann method

G. H. Tang, X. F. Li, and W. Q. Tao

Citation: Journal of Applied Physics **108**, 114903 (2010); doi: 10.1063/1.3517437
View online: http://dx.doi.org/10.1063/1.3517437
View Table of Contents: http://scitation.aip.org/content/aip/journal/jap/108/11?ver=pdfcov
Published by the AIP Publishing

Microannular electro-osmotic flow with the axisymmetric lattice Boltzmann method

G. H. Tang,[a] X. F. Li, and W. Q. Tao
State Key Laboratory of Multiphase Flow, School of Energy and Power Engineering, Xi'an Jiaotong University, Xi'an 710049, China

(Received 20 August 2010; accepted 21 October 2010; published online 7 December 2010)

Considering electro-osmotic flow in axisymmetric microducts is of both fundamental interest and practical significance. In this paper, an axisymmetric lattice Boltzmann model which solves the complete nonlinear Poisson–Boltzmann equation is presented to obtain the electric potential distribution in the electrolytes, and another axisymmetric lattice Boltzmann model is employed to solve the velocity field. First, the lattice Boltzmann model is validated by the electric potential distribution in the electrolyte with analytical solutions and finite volume method. Second, velocity distributions in circular tubes at various conditions are discussed. Then, we extend the lattice Boltzmann model for steady and pulsating electro-osmotic flow through annular microducts and the influences of inner to outer radius ratio, inner to outer zeta potential ratio and oscillating frequency are investigated. In addition, a numerical study of electro-osmotic flow in circular and annular microducts considering the non-Newtonian fluid behavior is also conducted for the first time. The results show that the microannular electro-osmotic flow exhibits much difference from the planar flow and the non-Newtonian rheology has significant effect on the flow behavior as well. © *2010 American Institute of Physics*. [doi:10.1063/1.3517437]

I. INTRODUCTION

Recently, the microfabrication technology has led to a rapid development of microelectromechanical systems (MEMS) and laboratory-on-a-Chip (LOC) devices.[1] The technological demands on microfluidic systems require a better understanding of the microscale fluidic phenomena. For microscale liquid flow, electrokinetic effect is one of the most important surface effects. In this study we focus on one of the electrokinetic phenomena, electroosmosis. Electro-osmotic flow (EOF) is generated due to the interactions of ions in the electrical double layer (EDL) with an externally applied electrical field.[2] Electroosmosis is a very promising nonmechanical technology for pumping, separating, and mixing in microdevices.[3] Due to its wide applications, EOF in microchannels has attracted much attention.[1–10]

The recent development of the lattice Boltzmann method has provided an alternative simulation tool for computational fluid dynamics.[11] Due to its distinctive advantages over conventional numerical methods, the lattice Boltzmann method has been successfully applied to different flows in science and engineering as an efficient and promising numerical method. Recently, the lattice Boltzmann method has been also found success in applications to microfluidics. Particularly, the lattice Boltzmann method has been successfully applied in modeling a range of microfluidic electro-osmotic applications.[12–16] However, some of studies employed a linearized Poisson–Boltzmann (PB) equation or solved the nonlinear PB equation with hybrid methods. These limitations are noted by many researchers,[3,6–8,10] and improved lattice Boltzmann models are proposed in succession. However, the existing lattice Boltzmann models for EOF are limited to parallel plate channels or parallel slits. Therefore, it is desirable to propose an axisymmetric lattice Boltzmann method for EOF in microducts. In addition, the flow behavior of non-Newtonian fluid in microannular ducts is of high interest in many areas of science and technology.[17] Fundamental understanding of the EOF of non-Newtonian fluid in microcircular and annular ducts is important to correctly predict the performance of microfluidic devices. In our previous work,[18] we studied EOF of non-Newtonian fluid in parallel microchannels. In this article, we extend the work to EOF of non-Newtonian fluid in circular and annular ducts using the present axisymmetric lattice Boltzmann method.

In recent years, the axisymmetric lattice Boltzmann method (LB) for axisymmetric flows has attracted much attention,[19–27] in which we found that Zhou's model[24] is fairly simple and efficient. Huang and Lu[28] recently also shown that Zhou's model seems to be the simplest one and this model is most stable in terms of τ sensitivity through theoretical and numerical analyses of three types of axisymmetric lattice Boltzmann models. In this regard, we employed Zhou's model to solve the velocity field. Note that some limitations still exist in the model such as neglecting azimuthal velocity, and containing some source terms involved with velocity gradients. Following the spirit of axisymmetric thermal lattice Boltzmann method in our previous work,[27] we develop an axisymmetric lattice Boltzmann model for the complete nonlinear PB equation to obtain the electric potential distribution in the electrolyte.

The rest of the paper is organized as follows. In Sec. II, the macroscopic governing equations for EOF are introduced. In Sec. III, we present the discrete Boltzmann equation for velocity field and electric potential. Section IV pre-

[a]Electronic mail: ghtang@mail.xjtu.edu.cn.

sents numerical results of electric potential and velocity distribution for EOF in circular tubes and annular ducts. A brief conclusion is presented at the end.

II. MACROSCOPIC HYDRODYNAMIC EQUATIONS FOR EOF

Consider an incompressible Newtonian aqueous electrolyte with ions continuously distributed in the whole microduct of radius R. The electric potential ψ at a point distance r from the axis can be described by the following Poisson equation in the cylindrical coordinate system:[29]

$$\nabla^2\psi(r) = \frac{1}{r}\frac{d}{dr}\left(r\frac{d\psi}{dr}\right) = -\frac{\rho_e(r)}{\varepsilon\varepsilon_0}, \tag{1}$$

where $\rho_e(r)$ is the net charge density at a point distance r from the axis, ε is the relative dielectric constant of the solution, and ε_0 is the permittivity of a vacuum. The ion distribution can be expressed by the Boltzmann equation

$$n_i = n_{i,\infty}\exp(-z_i e\psi/k_B T), \tag{2}$$

where $n_{i,\infty}$ is the ionic number concentration of ith species, z_i is the valence of type i ions, and n_∞ is the ionic number concentration in the bulk solution. The bulk ionic concentration n_∞ can be expressed as the product of the ionic molar concentration of c_∞ with the Avogadro's number of N_0, i.e., $n_\infty = c_\infty N_0$. Constant e is the charge of a proton, k_B is the Boltzmann constant, and T is the absolute temperature. For a symmetric electrolyte ($z_i = z$ and $n_{i,\infty} = n_\infty$) considered in this study, the net charge density can be expressed as

$$\rho_e(r) = -2n_\infty ze\sinh\left(\frac{z_i e\psi}{k_B T}\right). \tag{3}$$

Substituting Eq. (3) into Eq. (1) yields the nonlinear PB equation

$$\nabla^2\psi(r) = \frac{1}{r}\frac{d}{dr}\left(r\frac{d\psi}{dr}\right) = \frac{2n_\infty ze}{\varepsilon\varepsilon_0}\sinh\left(\frac{z_i e\psi}{k_B T}\right). \tag{4}$$

If the term $z_i e\psi/k_B T$ is small, we have $\sinh(z_i e\psi/k_B T) \approx z_i e\psi/k_B T$, which is known as Debye–Hückel approximation. Then Eq. (4) recovers the following linearized equation:

$$\nabla^2\psi(r) = \frac{1}{r}\frac{d}{dr}\left(r\frac{d\psi}{dr}\right) = \kappa^2\psi, \tag{5}$$

where $\kappa = (2n_\infty z^2 e^2/\varepsilon\varepsilon_0 k_B T)^{1/2}$, the reciprocal of Debye length. The boundary conditions on $\psi(r)$ are, as follows:

$$\left.\frac{d\psi(r)}{dr}\right|_{r=0} = 0 \quad \text{and} \quad \psi(r)|_{r=R} = \zeta, \tag{6}$$

where ζ is the zeta potential at the wall. Therefore, the solution of the linearized PB equation is[29,30]

$$\psi(r) = \zeta\frac{I_0(\kappa r)}{I_0(\kappa R)}, \tag{7}$$

where I_0 is the zero-order modified Bessel function of the first type. Equation (3) then becomes

$$\rho_e(r) = -\varepsilon\varepsilon_0\kappa^2\psi = -\varepsilon\varepsilon_0\kappa^2\zeta\frac{I_0(\kappa r)}{I_0(\kappa R)}. \tag{8}$$

When the cylindrical tube is applied with an external electric field along the axis direction, the motion of aqueous electrolyte is governed by the Navier–Stokes equations, which can be reduced to the following equation if assuming that the pure electrical driven flow is fully developed:

$$\rho\frac{\partial u}{\partial t} = \eta\frac{1}{r}\frac{\partial}{\partial r}\left(r\frac{\partial u}{\partial r}\right) + \rho_e(r)E_x, \tag{9}$$

where u is the streamwise velocity, η is the dynamic viscosity, ρ is the density of the fluid, ρ_e is the local net charge density, and E_x is the external electric field intensity applied along the axis direction. Considering the nonslip velocity at the wall and the geometry symmetry, the boundary conditions on $u(r)$ are, as follows:

$$\left.\frac{du(r)}{dr}\right|_{r=0} = 0 \quad \text{and} \quad u(r)|_{r=R} = 0. \tag{10}$$

The velocity $u(r)$ can be solved by combining Eq. (9) with Eqs. (8) and (10) for a steady-state flow:[29]

$$u(r) = -\frac{\varepsilon\varepsilon_0\zeta}{\eta}E_x\left[1 - \frac{I_0(\kappa r)}{I_0(\kappa R)}\right]. \tag{11}$$

III. NUMERICAL METHODS

A. The lattice Boltzmann equation for velocity field

In this study, the Zhou's axisymmetric lattice Boltzmann method is employed to solve the velocity field, the discrete evolution equation is[24]

$$f_\alpha(\mathbf{x} + \mathbf{c}_\alpha\delta_t, t + \delta_t) = f_\alpha(\mathbf{x}, t) - \frac{1}{\tau_v}(f_\alpha - f_\alpha^{eq}) + \frac{\delta_t}{\gamma c^2}c_{\alpha x}F_x, \tag{12}$$

where f is the single particle density distribution function and f^{eq} is the corresponding equilibrium distribution function, τ_v is the nondimensional relaxation time, $\mathbf{c}_\alpha$ is the particle discrete velocity. In this model, we have $c_0 = 0$, $c_\alpha = (\cos[(\alpha-1)\pi/2], \sin[(\alpha-1)\pi/2])c$ for $\alpha = 1,2,3,4$ and $c_\alpha = (\cos[(\alpha-5)\pi/2+\pi/4], \sin[(\alpha-5)\pi/2+\pi/4])\sqrt{2}c$ for $\alpha = 5,6,7,8$, where $c = \delta_x/\delta_t$ is the particle streaming speed (δ_x and δ_t are the lattice spacing and time step, respectively). $c_{\alpha x}$ is the particle's velocity in x link. γ is a constant, here $\gamma = 6$. F_x is the force term in x direction which is given by Eq. (13),[24]

$$F_x = \frac{\rho v}{r}\frac{\partial u}{\partial r} + E_x\rho_e(r). \tag{13}$$

The equilibrium density distribution function is defined as

$$f_\alpha^{eq} = \rho\omega_\alpha\left[1 + \frac{3}{c^2}(\mathbf{c}_\alpha\cdot\mathbf{u}) + \frac{9}{2c^4}(\mathbf{c}_\alpha\cdot\mathbf{u})^2 - \frac{3}{2c^2}(\mathbf{u}\cdot\mathbf{u})\right] \tag{14}$$

where $\omega_0 = 4/9$, $\omega_\alpha = 1/9$ for $\alpha = 1,2,3,4$ and $\omega_\alpha = 1/36$ for $\alpha = 5,6,7,8$. The macroscopic variables such as mass density and momentum density can be obtained by summing over the distribution function $f_\alpha(\mathbf{x}, t)$, as follows:

$$\rho = \sum_{\alpha} f_{\alpha} \quad \text{and} \quad \mathbf{u} = \sum_{\alpha} f_{\alpha}\mathbf{c}_{\alpha}/\rho. \tag{15}$$

The kinematic viscosity is

$$\nu = \frac{c^2\delta_t}{3}(\tau_v - 0.5). \tag{16}$$

B. The lattice Boltzmann equation for electric potential

Comparing the nonlinear PB equation [Eq. (4)] with the special case of the steady-state laminar incompressible energy equation when the velocity is zero and the thermal diffusivity is unity, we can derive the following discrete lattice Boltzmann evolution equation for the electric potential similar to the treatment of the energy equation in Ref. 27. One can refer to the appendix for details, as follows:

$$g_{\alpha}(\mathbf{x} + \mathbf{c}_{\alpha}\delta_t, t + \delta_t) - g_{\alpha}(\mathbf{x}, t) = -\omega_g[g_{\alpha}(\mathbf{x}, t) - g_{\alpha}^{eq}(\mathbf{x}, t)] + (1 - 0.5\omega_g)\delta_t S_1(\mathbf{x}, t), \tag{17}$$

where g is the distribution function and g^{eq} is the corresponding equilibrium distribution function, with $g_0^{eq} = 4\psi/9$, $g_{1,2,3,4}^{eq} = \psi/9$, $g_{5,6,7,8}^{eq} = \psi/36$. The potential diffusivity χ which is equal to unity in the simulations, is defined as

$$\chi = \frac{\delta_t \tau_g c^2}{3}. \tag{18}$$

The source term is chosen as

$$S_1 = -\frac{2n_{\infty}ze}{9\varepsilon\varepsilon_0}\sinh\left(\frac{ze\psi}{k_B T}\right). \tag{19}$$

ω_g is given by

$$\omega_g = [1 + (c_{\alpha r}\tau_g\delta_t/r)]/(\tau_g + 0.5). \tag{20}$$

The macroscopic electric potential in the liquid is calculated from Eq. (21) with an iteration method,

$$\psi = \sum_{\alpha} g_{\alpha} - 0.5\delta_t\frac{2n_{\infty}ze}{\varepsilon\varepsilon_0}\sinh\left(\frac{ze}{k_B T}\psi\right). \tag{21}$$

At the same time, we also derive the discrete lattice Boltzmann evolution equation for solving the linear PB equation [Eq. (5)], as follows:

$$g_{\alpha}(\mathbf{x} + \mathbf{c}_{\alpha}\delta_t, t + \delta_t) - g_{\alpha}(\mathbf{x}, t) = -\omega_g[g_{\alpha}(\mathbf{x}, t) - g_{\alpha}^{eq}(\mathbf{x}, t)] + (1 - 0.5\omega_g)\delta_t S_2(\mathbf{x}, t). \tag{22}$$

The corresponding source term is chosen as

$$S_2 = -\kappa^2 g_{\alpha}^{eq}. \tag{23}$$

The equilibrium distribution function, potential diffusivity, and ω_g are the same as mentioned above. The macroscopic electric potential under the Debye–Hückel approximation in the liquid is calculated from

$$\psi = \sum_{\alpha} g_{\alpha}/(1 + 0.5\delta_t\kappa^2). \tag{24}$$

Note that though there are some other sophisticated methods to solve the PB equation with high efficiency, such as conventional finite volume or finite difference numerical method, the convergence of the present lattice Boltzmann method is acceptable and the iterative computation reaches a local equilibrium within a short time. The present approach aids to solve all the equations within the same LBM framework, which is especially efficient for multiprocessor computing. Similar idea also appeared in Ref. 3 for parallel channel simulation. In addition, in this model, we use a uniform dielectric constant and neglect the fluctuations in the dielectric constant and thus the net charge density distribution in a symmetric electrolyte is proportional to the concentration difference between the cations and anions. This assumption is limited to small Peclet number less than one hundred when the ion-convection effect is insignificant compared to ion diffusion.

C. The boundary conditions for the lattice Boltzmann equations

Attention is now turned to the boundary conditions. Due to its kinetic nature and essential character of microscopic physics, the lattice Boltzmann method is of good capability for handling more general boundary conditions. Here we adopted the nonslip boundary conditions by Zou and He[31] on the upper and bottom walls to solve the density distribution function for velocity field. With regard to the lattice Boltzmann equation for the electric potential, the zeta potential on the upper and bottom walls are fixed in the simulation and Dirichlet boundary conditions are employed.[32] For the microcircular tube inlet and outlet, we employed periodic boundary conditions by assuming a fully developed flow.

IV. RESULTS AND DISCUSSION

A. The electro-osmotic potential distribution in the electrolytes

The electrolyte confined in a microcircular tube of radius $R = 2$ μm is considered. Unless otherwise mentioned in this paper, $\varepsilon\varepsilon_0 = 7.79 \times 10^{-10}$ C^2/(J m), $T = 293$ K, $e = 1.6 \times 10^{-19}$ C, $N_A = 6.02 \times 10^{23}$ mol^{-1}, $k_B = 1.38 \times 10^{-23}$ J/K, $\rho = 998.2$ kg/m^3, $z = +1$, and $\nu = 1.004 \times 10^{-6}$ m^2/s. Figure 1 shows the electric potential distribution across the pipe. In this case, the bulk ionic concentration is $c_{\infty} = 10^{-5}$ M. The solid symbols in the figure represent the analytical solutions of the linearized PB equation, the dashed lines represent LB results for the linearized PB equation, the solid lines represent the LB results for the nonlinear PB equation and the open symbols presents the results by numerically solving the nonlinear PB equation with our own developed code of the finite volume method (FVM). The electric potential in the electrolytes across the circular tube is decreasing from a given wall zeta potential (commonly assumed to be equal to the electrostatic surface potential), to zero around center zone. We can see that all the four results are in good agreement when the zeta potential is small, say, less than 50 mV in

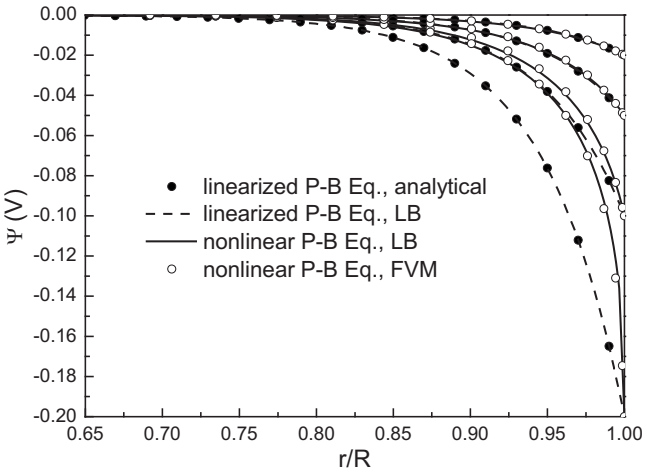

FIG. 1. The comparisons of electric potential distributions in a circular tube.

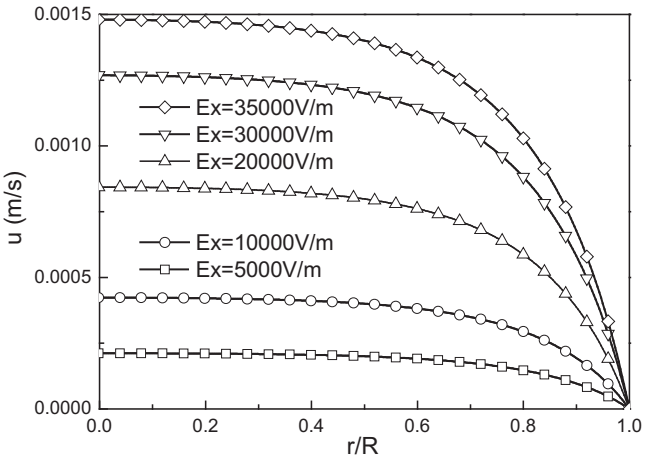

FIG. 3. Electro-osmotic velocity for various external electric fields.

the figure. However, the discrepancy between the nonlinear and linearized results increases as the zeta potential increases, though the LB results of the linearized equation still agree well with the linearized analytical solution, which confirms that the linearization of the PB equation is limited to small zeta potential. Our LB solutions for nonlinear PB equation are in good agreement with the macroscale FVM numerical results for all the cases.

B. EOF in circular tubes

We consider a steady flow driven by a uniform external electric field in a circular tube. The effects due to the variations of the ionic concentration, tube radius and external electric field are investigated with the present axisymmetric lattice Boltzmann method. A uniform external electric field E_x is applied along the axis direction of the tube $R=2$ μm. The zeta potential at the radius surface keeps at $\zeta=-50$ mV and the external electric field intensity keeps at $E_x=20\,000$ V/m. Figure 2 shows the streamwise velocity across the circular tube for the various ionic concentrations. From the upper to the bottom, the bulk ionic molar concentration is $c_\infty=10^{-3}$, 10^{-4}, 10^{-5}, 10^{-6}, 10^{-7}, and 10^{-8} M and the corresponding Debye length is 0.01, 0.032, 0.1, 0.32, 1, and 3.2 μm. Namely, as the bulk ionic concentration decreases, the Debye length increases. The velocity profiles across the tube resemble typical parabolas as the magnitude of the Debye length increases. From the figure we can also see that for the shown bulk ionic concentration range of $c_\infty=10^{-3}-10^{-6}$ M, the Debye length is small and the EDL is restricted to a very narrow region close to the wall. Therefore, the velocity increases sharply very near the wall and then almost keeps a constant in most of the tube region. More specifically, the ratio of the tube diameter to the Debye length is larger than about 10 for this bulk ionic concentration range of $c_\infty=10^{-3}-10^{-6}$ M.

The effect of external electric field on EOF is studied under the condition of the ionic concentration $c_\infty=10^{-6}$ M, zeta potential at radius surface $\zeta=-50$ mV and tube radius $R=2$ μm. The effect of external electric field on velocity profile is shown in Fig. 3. It is found that as the external electric field intensity increases, the EOF velocity almost increases proportionally.

Figure 4 shows the electro-osmotic velocity for various radii under the condition of the bulk ionic concentration $c_\infty=10^{-6}$ M, zeta potential $\zeta=-50$ mV and external electric field intensity $E_x=20\,000$ V/m. From Fig. 4 we find that the velocity distributions in the tube center region and the maximum velocity nearly keep a constant if the ratio of the tube diameter to the Debye length is larger than about 10 (R

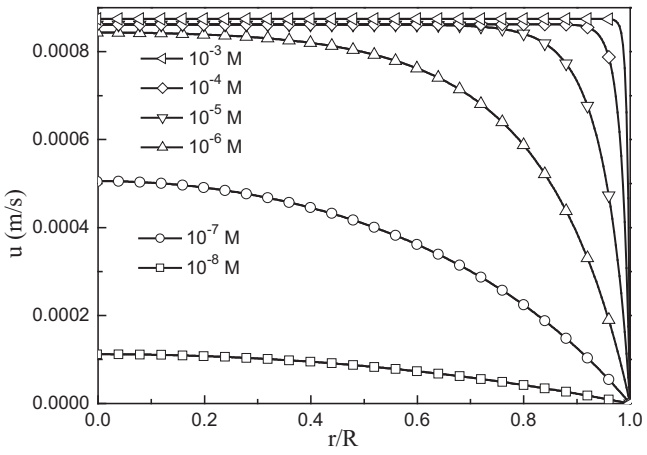

FIG. 2. Electro-osmotic velocity for various bulk ionic concentrations (c_∞).

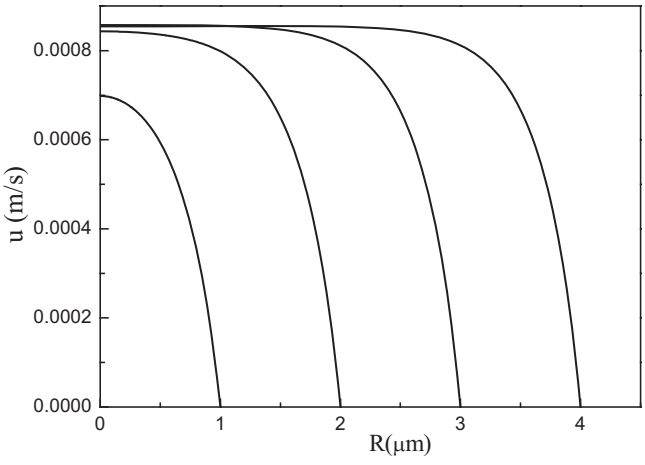

FIG. 4. Electro-osmotic velocity for various radii.

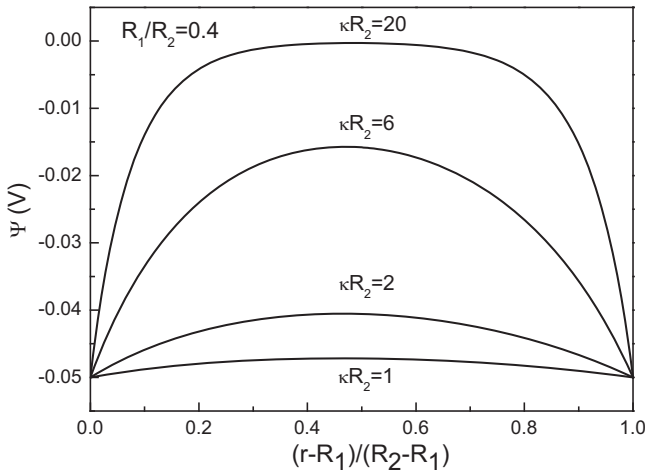

FIG. 5. The electrical potential distributions in annular ducts.

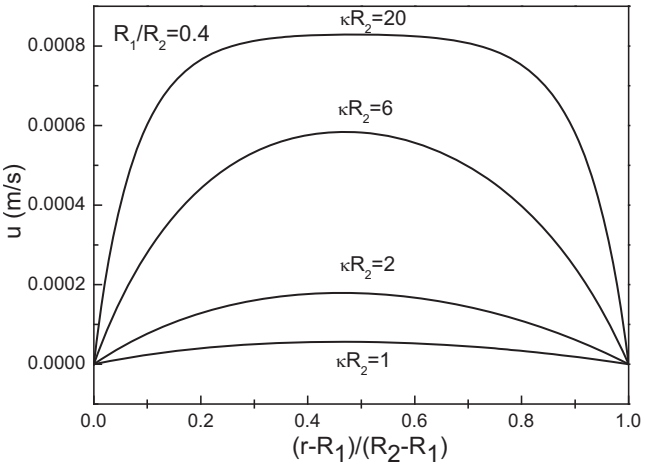

FIG. 6. The streamwise velocity profiles in annular ducts.

≥ 2 μm in Fig. 4). However, when the ratio gets small, the maximum velocity in the circular tube center drops down resulting from the overlapping of the electric double layers, since the Debye length measures the range of electrostatic influence of the single ions.

C. Steady EOF in annular ducts

The axisymmetric lattice Boltzmann method used above is also extended to simulate the EOF in annular ducts with the inner radius R_1 and outer radius R_2. The boundary conditions are that the inner circular wall is subjected to an electric potential ψ_1 and the outer circular wall with an electric potential ψ_2.

Consider EOF in an annular duct for $\psi_1=\psi_2=-50$ mV, $c_\infty=10^{-7}$ M, $R_2/R_1=0.4$, and $E_x=20\,000$ V/m. The distributions of electrical potential in the annulus are very important to the understanding of the flux in the annulus. Figure 5 shows the electric potential variation along the radial coordinate with different values of κR_2. Note that we use the dimensionless parameters, the inner to outer radius ratio R_1/R_2, the inner to outer zeta potential ratio ψ_1/ψ_2, and the ratio of radius to Debye length κR_2 due to the impact of multiparameter in annular ducts. It is found that the electric potential profiles across the annulus develop sharp features in the near vicinity of the wall as κR_2 increases. The electric potential gets smaller as κR_2 decreases. This phenomenon is also caused by the overlapping of Debye layers from the inner surface and the outer surface when the annulus gap becomes smaller. Figure 6 shows the corresponding velocity profiles for various κR_2. From the figure we can see that as κR_2 increases, the velocity profiles across the tube also develop sharp features in the near vicinity of the wall and then keep a constant nearly in most of the annulus region when the value of κR_2 is large ($\kappa R_2=20$ in the figure). While the velocity profiles across the annulus present to be typical parabolas when the magnitude of κR_2 is small.

Figures 7 and 8 show the electric potential distribution in annular ducts when the inner and outer surfaces have different zeta potentials. From these figures, we can see that the electric potential along the radial direction at a certain point becomes smaller as the ratio of inner radius to outer radius decreases. Figure 7 shows the electric potential distribution in annular duct at a large $\kappa R_2=10$. We can see that when the radius ratio is small, the magnitude of electric potential decreases first and then increases from the surface with smaller zeta potential to the other surface with larger zeta potential. However, for large radius ratio [$R_1/R_2=0.9$ in Fig. 7(a) and

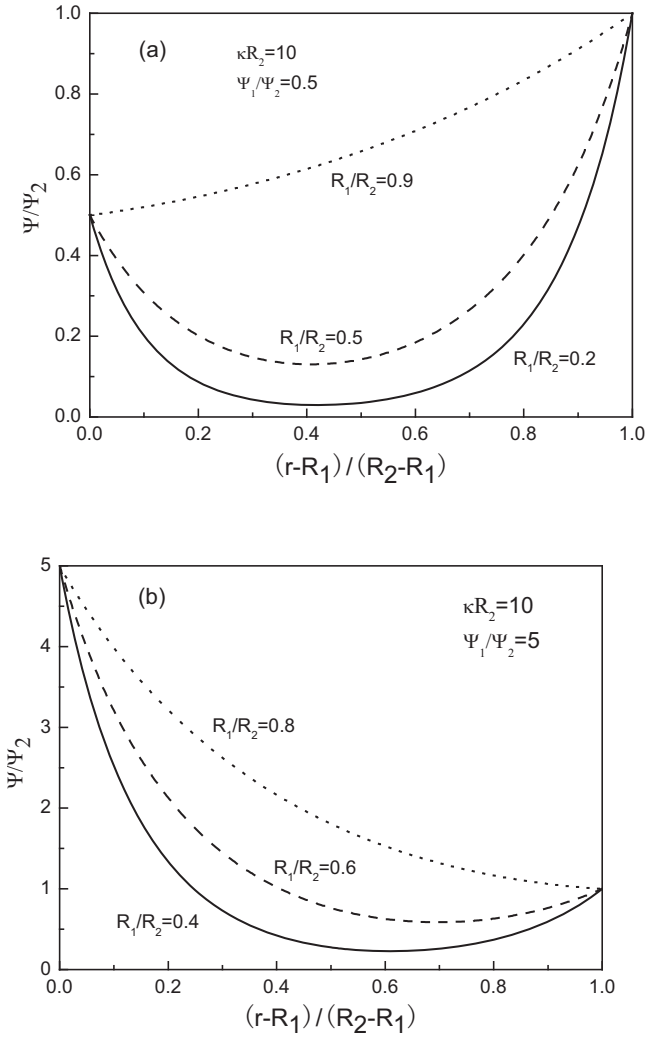

FIG. 7. Electric potential distribution in annular ducts at $\kappa R_2=10$. (a) $\psi_1/\psi_2=0.5$. (b) $\psi_1/\psi_2=5$.

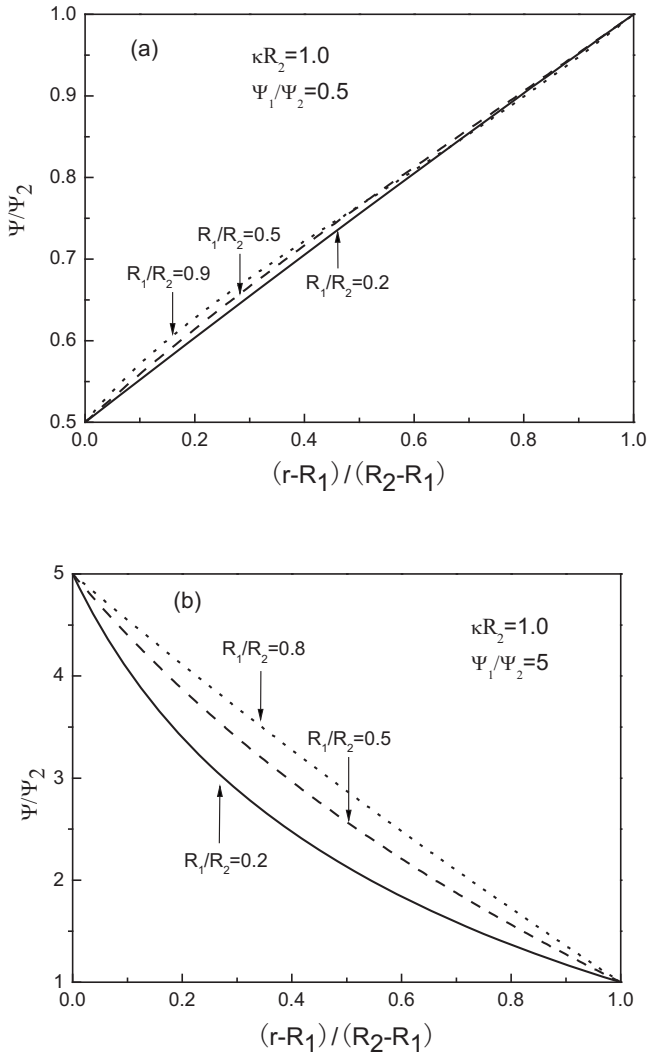

FIG. 8. Electric potential distribution in annular ducts at $\kappa R_2=1.0$. (a)$\psi_1/\psi_2=0.5$. (b) $\psi_1/\psi_2=5$.

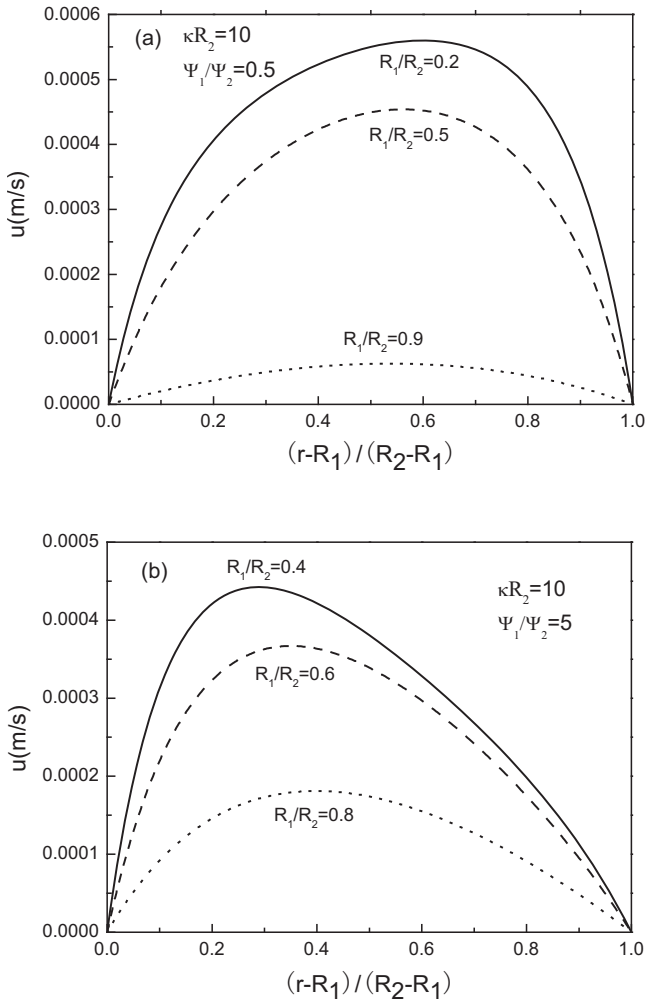

FIG. 9. Velocity profiles in annular ducts at $\kappa R_2=10$. (a)$\psi_1/\psi_2=0.5$. (b) $\psi_1/\psi_2=5$.

$R_1/R_2=0.8$ in Fig. 7(b)], the electric potential always increases from the surface with lower zeta potential to the surface with larger zeta potential. Figure 8 shows the electric potential distribution in annular duct at a small $\kappa R_2=1$. We can see that the magnitude of electric potential always increases from the surface with smaller zeta potential to the other surface with larger zeta potential at the shown radius ratios. Comparing Fig. 7 with Fig. 8, we can see that at large κR_2 the differences in the electric potential among different ratios of inner to outer radius are more significant than those at small κR_2. The results are in good agreement with those reported in Ref. 33.

Figures 9 and 10 show the corresponding velocity profiles in annular ducts. We find that the streamwise velocity becomes smaller as the ratio of inner radius to outer radius increases. There occurs a maximum velocity for every radius ratio. This maximum is closer to the radius surface with a larger zeta potential but approaches the midpoint between cylinders as the gap R_2-R_1 becomes small (i.e., the radius ratio of R_1/R_2 increases). In addition, as the gap becomes small, the velocity profile approaches a parabolic distribution. Comparing Fig. 10 (small $\kappa R_2=1$) with Fig. 9 (large $\kappa R_2=10$), we can see that at small κR_2 the maximum velocity appears closer to the annulus midpoint for the same radius ratio.

D. Electro-osmotic pulsating flow in annular ducts

We study the EOF flow in annular microducts by changing the polarity of the externally imposed electric field. We used very high frequency electric fields to drive the flow. The time periodic external electric intensity is

$$E_x = \mathrm{Re}[E_0 e^{i\omega t}], \tag{25}$$

with an amplitude E_0 and a frequency $\omega=2\pi/(T_E\delta_t)$. In the simulations, the time step is $\delta_t=2.7\times10^{-12}$ s, and T_E represents the period of the externally imposed electric field normalized by δ_t. The bulk ionic concentration is $c_\infty=10^{-4}$ M and the corresponding Debye length is 0.032 μm. The ratio of inner radius R_1 to outer radius R_2 is 0.4, and the external electric field is $E_x=20\,000$ V/m.

In Fig. 11, the electric potential at the inner and outer wall both keeps the same at $\psi_1=\psi_2=-50$ mV. From Figs. 11(a)–11(c), as the applied frequency increases, the perturbed flow region becomes smaller. For the lower frequency the velocity perturbation propagates from the near-wall region deeper into the bulk region while for even higher fre-

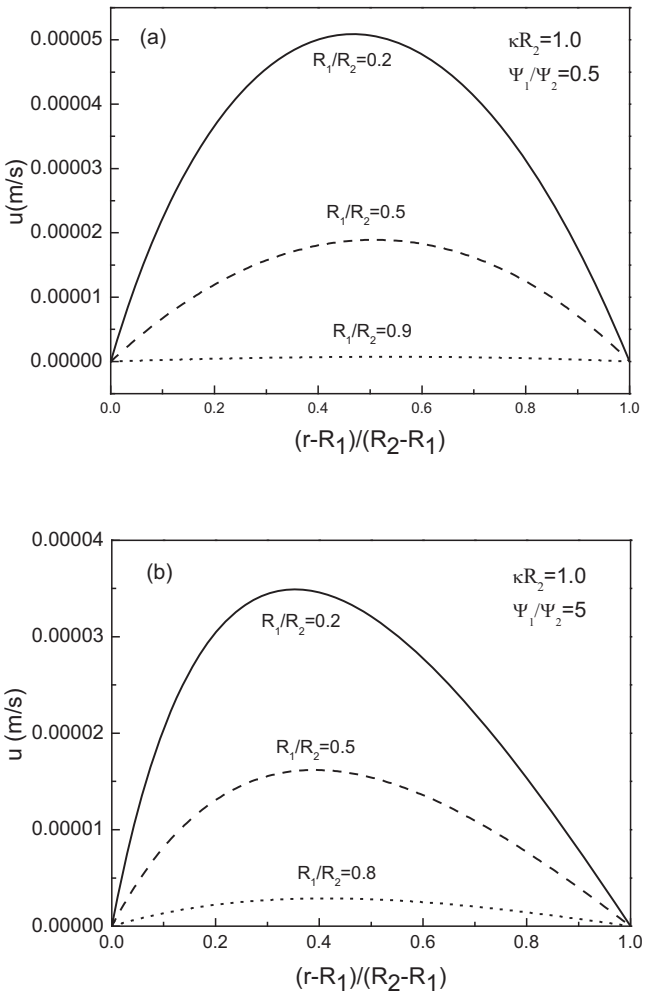

FIG. 10. Velocity profiles in annular ducts at $\kappa R_2=1.0$. (a)$\psi_1/\psi_2=0.5$. (b) $\psi_1/\psi_2=5$.

quency, the flow in center region remains virtually unperturbed. This phenomenon is attributed to that when the frequency is very high, the electric field changes its direction quite rapidly and the fluid cannot respond fast enough due to its finite inertia. The diffusion time scale is greater than the oscillation time period and hence no sufficient time for the flow momentum in the double layer to diffuse into the bulk fluid region. Consequently the perturbed area is restricted within a thin layer close to the wall. Comparing Fig. 11(d) with Fig. 11(c) which is applied with the same frequency but different Debye length, we can see that as the Debye length increases in Fig. 11(d), the EDL effect extends deeper to the fluid bulk region.

We also investigated the above case when $\psi_1/\psi_2=5$ and $\psi_1/\psi_2=0.5$, respectively. As Fig. 12(a) shown, the velocity amplitude near the inner circular wall is larger than that near the outer circular wall, which results from the fact that the larger wall electric potential generates the larger electro-osmotic force. On the contrary, the velocity amplitude near the inner circular wall is smaller than that near the outer circular wall for $\psi_1/\psi_2=0.5$ shown in Fig. 12(b). Similarly, due to the ratio of Debye length to annulus gap is very small, the EDL effect is restricted close to the wall surface and most of the bulk region is unperturbed. The presented EOF pulsating results would be useful in practical applications of controlling mass flow rate or species mixing.

E. EOF of non-Newtonian fluid

The electro-osmotic flows studied above are limited to Newtonian fluid. In this section, we investigate flow of non-Newtonian fluid in circular and annular pipes using the present modified axisymmetric lattice Boltzmann model. In the commonly used power-law model for non-Newtonian fluid, the viscosity is given by

$$\eta = \eta_0 \dot{\gamma}^{n-1}, \tag{26}$$

where the shear rate related $\dot{\gamma}$ is $\dot{\gamma}=|du/dr|$ and the parameter n is the power-law exponent which determines the response of the fluid to change in shear rate. The fluid is shear thinning for $n<1$, shear thickening for $n>1$ and Newtonian fluid with shear-independent viscosity η_0 for $n=1$. Coupling Eqs. (16) and (26), together with $\eta=\rho\nu$, we have a shear-dependent relaxation time τ_ν at each node in the lattice Boltzmann evolution Eq. (12).

A simple electro-osmotic driven non-Newtonian fluid flow in microcircular tube of radius $R=2$ μm is considered. In the simulation, we choose $\varepsilon\varepsilon_0=7.79\times10^{-10}$ $C^2/(J\,m)$, $T=293$ K, $e=1.6\times10^{-19}$ C, $N_A=6.02\times10^{23}$ mol^{-1}, $k_B=1.38\times10^{-23}$ J/K, $\rho=1000$ kg/m^3, $z=+1$, and $\nu=1.004\times10^{-6}$ m^2/s, the surface zeta potential of $\zeta=-50$ mV, and the externally applied electric field intensity of $E_x=20\,000$ V/m. The treatment of the boundary conditions is the same as the Newtonian fluid flow in circular pipe.

Figures 13(a) and 13(b) present the normalized streamwise velocity profile along the diameter of pipe for $c_\infty=10^{-8}$ M and $c_\infty=10^{-5}$ M, respectively. From the figure, we can see that for the Newtonian fluid of $n=1$, the velocity profile is parabolic at lower ionic concentration, which resembles a typical pressure-driven flow. However, as the bulk ionic concentration increases, the velocity profile transits from parabolic to pluglike. The velocity profiles for non-Newtonian flow of $n=1.3$ and $n=1.5$ show curvature and sharplike around the center peak velocity while the case of $n=0.6$ presents typical plug flow for $c_\infty=10^{-8}$ M. The velocity profiles for non-Newtonian flow of $n=1.2$ and $n=1.4$ show curvature and sharplike around the center peak velocity while the case of $n=0.6$ presents typical plug flow for $c_\infty=10^{-5}$ M. The velocity profiles for all the values of n exhibit more flattening at $c_\infty=10^{-5}$ M compared to $c_\infty=10^{-8}$ M. These different flow profiles are caused by variations in the Debye length. The calculated Debye length for $c_\infty=10^{-5}$ M is 0.10113 μm, compared to 3.19747 μm for $c_\infty=10^{-8}$ M.

We also studied the electro-osmotic driven non-Newtonian fluid flow in microannular tube of fixed outer radius $R_2=5$ μm. The other parameters here are the same as the above case. As shown in Fig. 14, for $n=0.6$ we observe a general flattening of the velocity profile. Conversely, the profiles for $n=1.2$ and $n=1.4$ show great curvature near the center peak velocity, and the larger exponent n, the greater curvature. From Figs. 14(a) and 14(b), the velocity profiles for all the values of n exhibit more flattening at c_∞

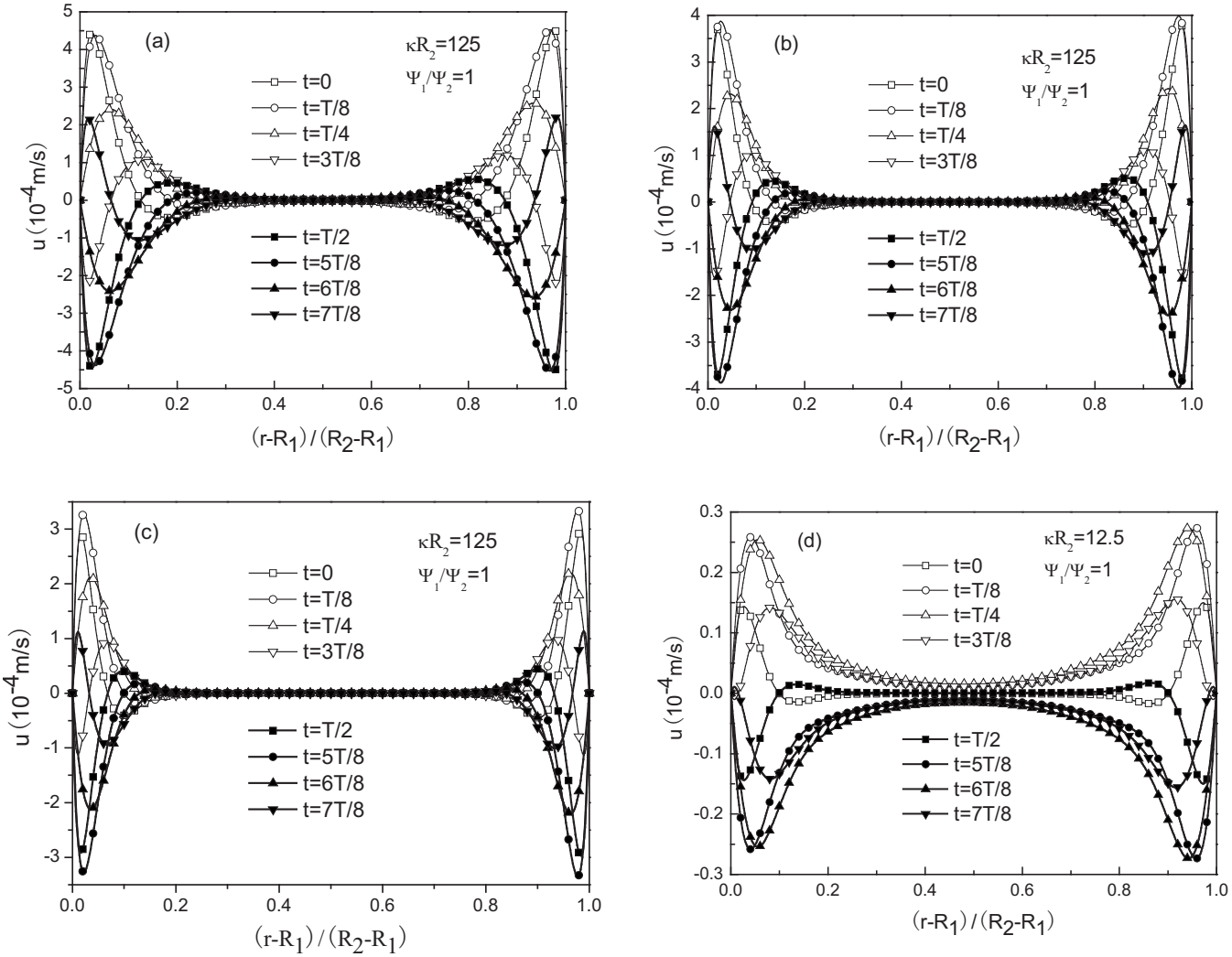

FIG. 11. The velocity distribution for pulsating EOF in annular ducts at different times. (a) $T_E=80\,000$, $\kappa R_2=125$. (b) $T_E=40\,000$, $\kappa R_2=125$. (c) $T_E=20\,000$, $\kappa R_2=125$. (d) $T_E=20\,000$, $\kappa R_2=12.5$.

$=10^{-5}$ M compared to $c_\infty=10^{-8}$ M. In Fig. 14(c) we can see that the velocity profile leans from the inner surface to the annulus center as the value of n increases. Comparing Fig. 14(c) with Fig. 14(a), we can see that the velocity profile leans toward the inner cylinder as the radius ratio of inner radius to outer radius decreases.

V. CONCLUSIONS

Motivated by the growing interest in electroosmosis as a reliable no moving parts strategy to pump liquid, to mix liquid, and to control fluid motion in microfluidic devices, we have numerically studied steady-state and pulsating EOF in circular and annular microducts. We have developed an axisymmetric lattice Boltzmann model, which recovers the complete nonlinear PB equation, to solve the electric potential distribution in the electrolytes. And we used another axisymmetric lattice Boltzmann model, which recovers the incompressible Navier–Stokes equation, to solve the velocity field. We have validated the method by the electric potential distribution with analytical solutions and FVM numerical results.

We first applied this method for EOF in circular tubes. By studying the effects of the bulk ionic concentration, external electric field and tube radius, we find that the velocity profiles exhibit a sharp variation adjacent to the walls and the maximum velocity nearly keeps a constant in most of the tube center regions if the ratio of the tube diameter to the Debye length is larger than about 10.

For EOF in annular tubes, we find that both the electric potential distribution and the velocity are influenced by the ratio of inner radius to outer radius R_1/R_2, the value of ψ_1/ψ_2, and the Debye length. For the electro-osmotic pulsating flow in annular tubes, the ratio of the annulus gap to Debye length has a significant effect on the velocity amplitude and most of the bulk fluid is unperturbed if this ratio is large. When the frequency is small, the velocity perturbation propagates from the near-wall region deeper into the bulk region. However, for the cases of large frequency, the perturbed area is restricted within a thin layer very close to the radius wall.

The non-Newtonian effect on EOF has also been investigated. For electro-osmotic driven non-Newtonian fluid flow in circular pipes, our investigation shows that the velocity

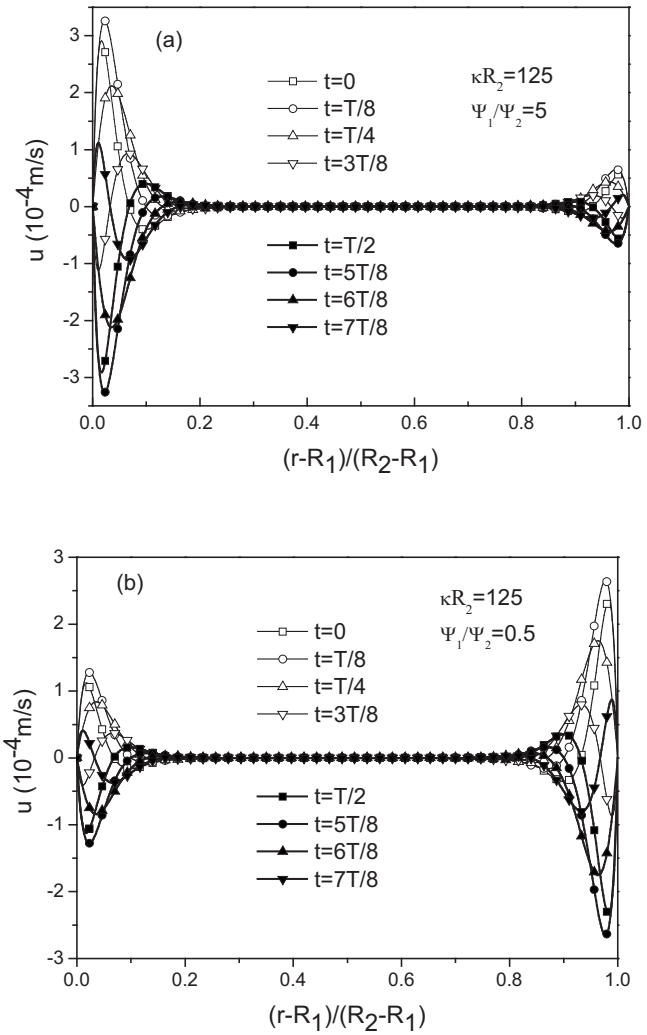

FIG. 12. The velocity distribution for pulsating EOF in annular ducts at different times. (a) $T_E=20\,000$, $\psi_1=-50$ mV, and $\psi_2=-10$ mV. (b) $T_E=20\,000$, $\psi_1=-20$ mV, and $\psi_2=-40$ mV.

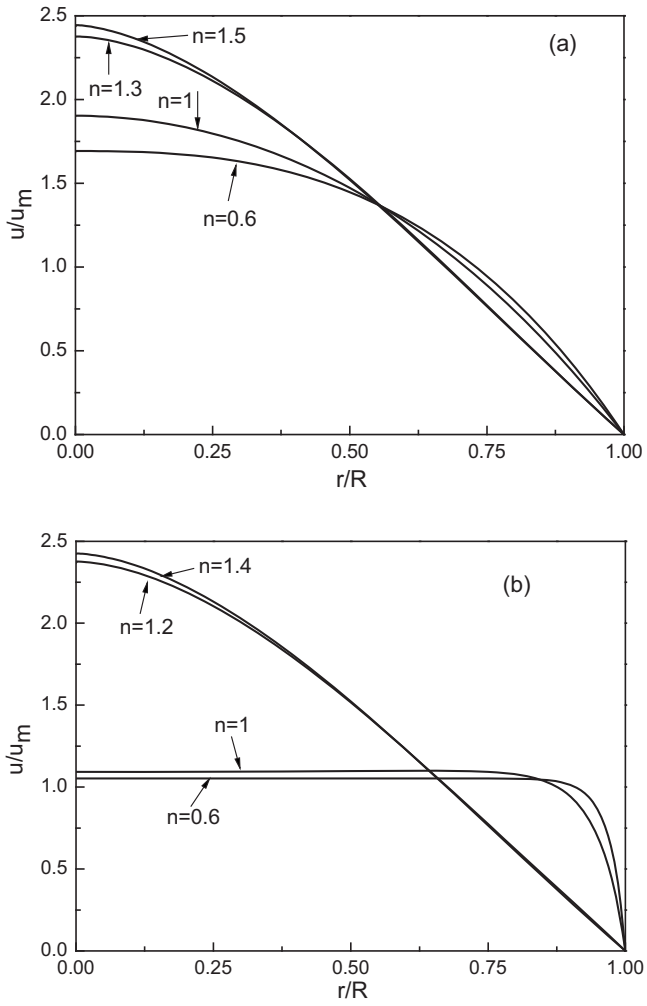

FIG. 13. Normalized electro-osmotic velocity profiles in a circular tube for various power-law exponents n at two different ionic concentrations. (a) $c_\infty=10^{-8}$ M. (b) $c_\infty=10^{-5}$ M.

profile is dominated by the fluid rheological behavior. The shear thickening fluid is more difficult to grow into a pluglike flow than Newtonian. In contrast, the shear thinning fluid is more inclined to develop into the pluglike flow. For the flow in annular ducts, the velocity profile is significantly dependent on the ratio of inner radius to outer radius R_1/R_2 as well. The present results demonstrate that the present axisymmetric lattice Boltzmann method can be used as an effective numerical tool for studying the EOF in annular microducts. The results obtained from this work not only can provide insights into the EOF but also can aid in predicting EOF mass flow rate or species mixing in practical applications of electrokinetic micropumps or micromixers.

ACKNOWLEDGMENTS

The authors would like to thank the National Natural Science Foundation of China for the support under Grant No. 50776067, the Science and Technology Research Development Program of Shaanxi Province for the support under Grant No. 2010KJXX-01, and the Program for NCET in university for the support under the Grant no. NCET-07-0676.

APPENDIX: RECOVERING THE MACROSCOPIC PB EQUATION THROUGH THE CHAPMAN–ENSKOG PROCEDURE

In the appendix, we present the detailed mathematic derivation of Eq. (4) from Eq. (17) through the Chapman–Enskog procedure. In order to recover Eq. (4), we first introduce the following evolution equation:

$$
\begin{aligned}
&g_\alpha(\mathbf{x}+\mathbf{c}_\alpha\delta_t,t+\delta_t)-g_\alpha(\mathbf{x},t)\\
&=-\frac{1}{2\tau_g}[g_\alpha(\mathbf{x}+\mathbf{c}_\alpha\delta_t,t+\delta_t)-g_\alpha^{eq}(\mathbf{x}+\mathbf{c}_\alpha\delta_t,t+\delta_t)]\\
&\quad-\frac{1}{2\tau_g}[g_\alpha(\mathbf{x},t)-g_\alpha^{eq}(\mathbf{x},t)]\\
&\quad-\frac{\mathbf{c}_{\alpha r}}{r}\delta_t[g_\alpha(\mathbf{x},t)-g_\alpha^{eq}(\mathbf{x},t)]\\
&\quad+\frac{\delta_t}{2}[S_1(\mathbf{x}+\mathbf{c}_\alpha\delta_t,t+\delta_t)-S_1(\mathbf{x},t)],
\end{aligned}
\tag{A1}
$$

where g_α is the electric potential distribution function, τ_g is nondimensional relaxation time, S_1 is source term, $\mathbf{c}_\alpha=(c_{\alpha x},c_{\alpha r})$ is the discrete velocities, and g_α^{eq} is the corresponding equilibrium distribution function, with $g_0^{eq}=4\psi/9$,

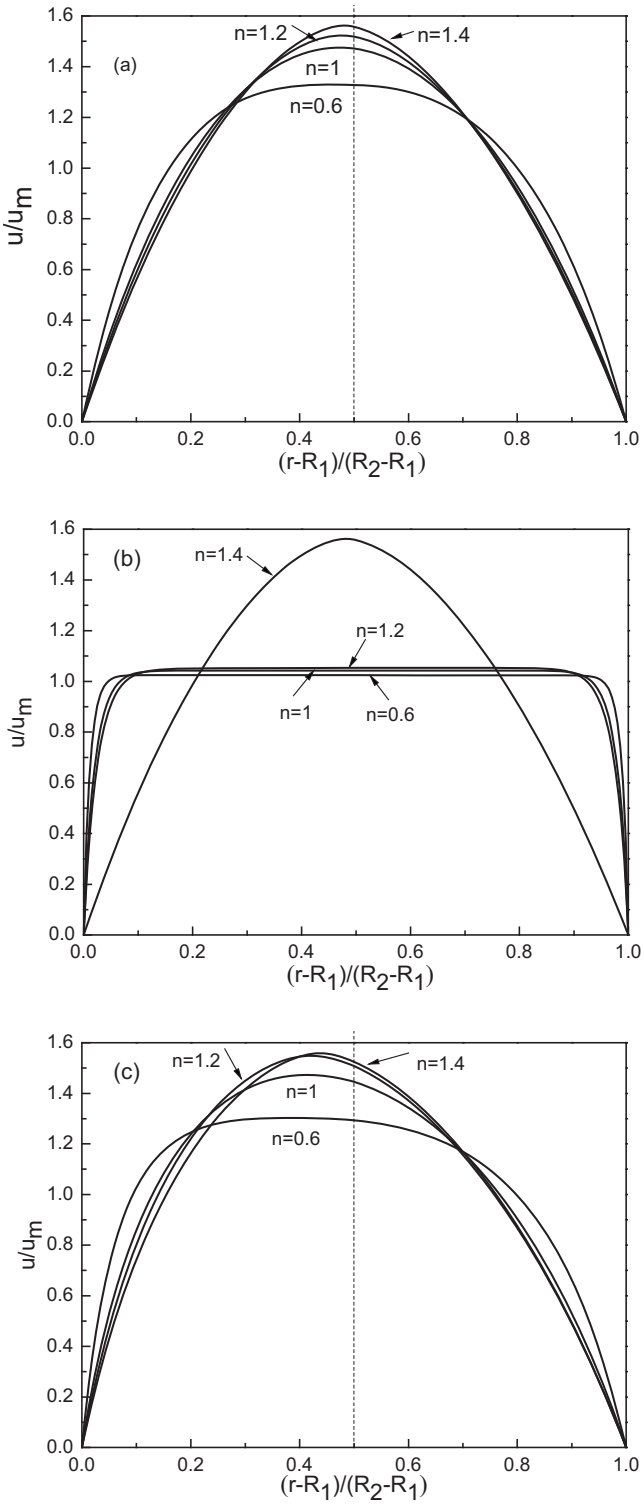

FIG. 14. Normalized electro-osmotic velocity profiles for power-law flow in annular ducts. (a) $R_1/R_2=0.5$, $c_\infty=10^{-8}$ M. (b) $R_1/R_2=0.5$, $c_\infty=10^{-5}$ M. (c) $R_1/R_2=0.09$, $c_\infty=10^{-8}$ M.

$g^{eq}_{1,2,3,4}=\psi/9$, $g^{eq}_{5,6,7,8}=\psi/36$. It can be found that

$$\sum_\alpha g^{eq}_\alpha=\psi,\quad \sum_\alpha c_{\alpha i}g^{eq}_\alpha=0,\quad \sum_\alpha c_{\alpha i}c_{\alpha j}g^{eq}_\alpha=c_s^2\psi\delta_{ij}, \tag{A2}$$

where c_s is the sound speed. Through the second-order Taylor-series expansion, the evolution Eq. (A1) can be reduced to

$$\delta_t(\partial_t+\mathbf{c}_\alpha\cdot\nabla)g_\alpha+\frac{\delta_t^2}{2}(\partial_t+\mathbf{c}_\alpha\cdot\nabla)^2g_\alpha=-\frac{1}{\tau_g}(g_\alpha-g^{eq}_\alpha)$$
$$-\frac{\delta_t}{2\tau_g}(\partial_t+\mathbf{c}_\alpha\cdot\nabla)(g_\alpha-g^{eq}_\alpha)-\frac{c_{\alpha r}}{r}\delta_t(g_\alpha-g^{eq}_\alpha)+\delta_tS_1$$
$$+\frac{\delta_t^2}{2}(\partial_t+\mathbf{c}_\alpha\cdot\nabla)S_1. \tag{A3}$$

Introducing the following multiscale expansions:

$$\partial_t=\partial_{t0}+\delta_t\partial_{t1},\quad g_\alpha=g^{(0)}_\alpha+\delta_tg^{(1)}_\alpha+\delta_t^2g^{(2)}_\alpha, \tag{A4}$$

and substituting Eq. (A4) into Eq. (A3), Eq. (A3) to order $(\delta_t)^0$ is

$$g^{(0)}_\alpha=g^{eq}_\alpha, \tag{A5}$$

to order $(\delta_t)^1$ is

$$(\partial_{t0}+\mathbf{c}_\alpha\cdot\nabla)g^{(0)}_\alpha+\frac{1}{\tau_g}g^{(1)}_\alpha=S_1, \tag{A6}$$

and to order $(\delta_t)^2$ is

$$\partial_{t1}g^{(0)}_\alpha+(\partial_{t0}+\mathbf{c}_\alpha\cdot\nabla)g^{(1)}_\alpha+\frac{1}{2}(\partial_{t0}+\mathbf{c}_\alpha\cdot\nabla)^2g^{(0)}_\alpha+\frac{1}{\tau_g}g^{(2)}_\alpha$$
$$+\frac{1}{2\tau_g}(\partial_{t0}+\mathbf{c}_\alpha\cdot\nabla)g^{(1)}_\alpha=-\frac{c_{\alpha r}}{r}g^{(1)}_\alpha$$
$$+\frac{1}{2}(\partial_{t0}+\mathbf{c}_\alpha\cdot\nabla)S_1. \tag{A7}$$

Applying Eq. (A6), we can rewrite Eq. (A7) as

$$\partial_{t1}g^{(0)}_\alpha+(\partial_{t0}+\mathbf{c}_\alpha\cdot\nabla)g^{(1)}_\alpha+\frac{1}{\tau_g}g^{(2)}_\alpha=-\frac{c_{\alpha r}}{r}g^{(1)}_\alpha. \tag{A8}$$

Taking the summations of Eqs. (A6) and (A8), we can obtain

$$\partial_{t0}\psi=\sum_\alpha S_1, \tag{A9}$$

$$\partial_{t1}\psi+\partial_i\left(\sum_\alpha c_{\alpha i}g^{(1)}_\alpha\right)=-\frac{1}{r}\sum_\alpha c_{\alpha r}g^{(1)}_\alpha. \tag{A10}$$

In order to recover the macroscopic Eq. (4), $\Sigma_\alpha S_1$ should be given by $\Sigma_\alpha S_1=-(2n_\infty ze/\varepsilon\varepsilon_0)\sinh(ze\psi/k_BT)$, and we have

$$S_1=-\frac{2n_\infty ze}{9\varepsilon\varepsilon_0}\sinh\left(\frac{ze\psi}{k_BT}\right), \tag{A11}$$

where ψ is the value of the previous iteration step, so S_1 is a determined value.

From Eq. (A6), we have

$$\sum_\alpha c_{\alpha i}g^{(1)}_\alpha=-\tau_g\partial_j\sum_\alpha c_{\alpha i}c_{\alpha j}g^{(0)}_\alpha. \tag{A12}$$

From Eqs. (A2) and (A5), we can obtain

$$\partial_j\sum_\alpha c_{\alpha i}c_{\alpha j}g^{(0)}_\alpha=c_s^2\partial_i\psi. \tag{A13}$$

Therefore, Eq. (A12) can be reduced to

$$\sum_{\alpha} c_{\alpha i} g_{\alpha}^{(1)} = -\tau_g c_s^2 \partial_i \psi. \tag{A14}$$

Substituting Eq. (A14) into Eq. (A10) and then combing Eq. (A9) with Eq. (A10), we can obtain the following macroscopic electric potential equation:

$$\partial_t \psi = \partial_i(\chi \partial_i \psi) + \chi \frac{1}{r} \partial_r \psi - \frac{2 n_\infty z e}{\varepsilon \varepsilon_0} \sinh\left(\frac{z_i e \psi}{k_B T}\right), \tag{A15}$$

where the potential diffusivity χ is given by $\chi = \delta_t \tau_g c_s^2$. If assuming that the steady-state pure electrical driven flow is fully developed and the potential diffusivity χ is equal to unity, Eq. (A15) can be reduced to

$$\frac{1}{r}\frac{d}{dr}\left(r\frac{d\psi}{dr}\right) = \frac{2 n_\infty z e}{\varepsilon \varepsilon_0} \sinh\left(\frac{z_i e \psi}{k_B T}\right). \tag{A16}$$

To eliminate the implicitness of Eq. (A1), a distribution function $\bar{g}_\alpha = g_\alpha + 0.5(g_\alpha - g_\alpha^{eq})/\tau_g - 0.5\delta_t S_1$ can be shown. Through some standard algebra, the evolution equation for $\bar{g}_\alpha$ can be obtained,

$$\bar{g}_\alpha(\mathbf{x} + \mathbf{c}_\alpha \delta_t, t + \delta_t) - \bar{g}_\alpha(\mathbf{x}, t) = -\omega_g[\bar{g}_\alpha(\mathbf{x}, t) - g_\alpha^{eq}(\mathbf{x}, t)] + (1 - 0.5\omega_g)\delta_t S_1(\mathbf{x}, t). \tag{A17}$$

where ω_g is given by $\omega_g = [1 + (c_{\alpha r}\tau_g \delta_t / r)]/(\tau_g + 0.5)$. The macroscopic electric potential ψ can be calculated with an iteration method as

$$\psi = \sum_{\alpha} \bar{g}_\alpha - 0.5\delta_t \frac{2 n_\infty z e}{\varepsilon \varepsilon_0} \sinh\left(\frac{z e}{k_B T}\psi\right). \tag{A18}$$

For simplicity, we use g instead of $\bar{g}$ in the paper.

[1] D. Q. Li, *Electrokinetics in Microfluidics* (Elsevier Academic, Boston, 2004).
[2] C. M. Hou, *Microflows and Nanoflows Fundamentals and Simulation* (Springer, New York, 2005).
[3] J. K. Wang, M. R. Wang, and Z. X. Li, J. Colloid Interface Sci. **296**, 729 (2006).
[4] L. Q. Ren and D. Q. Li, J. Colloid Interface Sci. **243**, 255 (2001).
[5] Y. H. Zhang, X. J. Gu, R. W. Barber, and D. R. Emerson, J. Colloid Interface Sci. **275**, 670 (2004).
[6] Z. L. Guo, T. S. Zhao, and Y. Shi, J. Chem. Phys. **122**, 144907 (2005).
[7] G. H. Tang, Z. Li, J. K. Wang, Y. L. He, and W. Q. Tao, J. Appl. Phys. **100**, 094908 (2006).
[8] Z. H. Chai, Z. L. Guo, and B. C. Shi, J. Appl. Phys. **101**, 104913 (2007).
[9] J. Wu, J. Appl. Phys. **103**, 024907 (2008).
[10] G. H. Tang, Y. L. He, and W. Q. Tao, J. Appl. Phys. **107**, 104906 (2010).
[11] S. Chen and G. Doolen, Annu. Rev. Fluid Mech. **30**, 329 (1998).
[12] P. B. Warren, Int. J. Mod. Phys. C **8**, 889 (1997).
[13] B. M. Li and D. Y. Kwok, J. Chem. Phys. **120**, 947 (2004).
[14] F. Z. Tian and D. Y. Kwok, Langmuir **21**, 2192 (2005).
[15] S. Melchionna and S. Succi, J. Chem. Phys. **120**, 4492 (2004).
[16] F. Capuani, I. Pagonabarraga, and D. Frenkel, J. Chem. Phys. **121**, 973 (2004).
[17] W. T. Kim, H. G. Chen, and M. S. Jhon, J. Appl. Phys. **99**, 08N106 (2006).
[18] G. H. Tang, X. F. Li, Y. L. He, and W. Q. Tao, J. Non-Newtonian Fluid Mech. **157**, 133 (2009).
[19] I. Halliday, L. A. Hammond, C. M. Care, K. Good, and A. Stevens, Phys. Rev. E **64**, 011208 (2001).
[20] T. Lee, H. Huang, and C. Shu, Int. J. Mod. Phys. C **17**, 645 (2006).
[21] H. Huang, T. Lee, and C. Shu, Int. J. Numer. Methods Heat Fluid Flow **17**, 587 (2007).
[22] T. Reis and T. N. Phillips, Phys. Rev. E **75**, 056703 (2007).
[23] T. Reis and T. N. Phillips, Phys. Rev. E **77**, 026703 (2008).
[24] J. G. Zhou, Phys. Rev. E **78**, 036701 (2008).
[25] S. Chen, J. Tolke, S. Geller, and M. Krafczyk, Phys. Rev. E **78**, 046703 (2008).
[26] Z. L. Guo, H. F. Han, B. C. Shi, and C. G. Zheng, Phys. Rev. E **79**, 046708 (2009).
[27] Q. Li, Y. L. He, G. H. Tang, and W. Q. Tao, Phys. Rev. E **80**, 037702 (2009).
[28] H. B. Huang and X. Y. Lu, Phys. Rev. E **80**, 016701 (2009).
[29] S. Chakraborty and S. Ray, Phys. Fluids **20**, 083602 (2008).
[30] C. Rice and R. Whitehead, J. Phys. Chem. **69**, 4017 (1965).
[31] Q. Zou and X. He, Phys. Fluids **9**, 1591 (1997).
[32] G. H. Tang, W. Q. Tao, and Y. L. He, Phys. Rev. E **72**, 016703 (2005).
[33] R. C. Wu and K. D. Papadopoulos, Colloids Surf., A **161**, 469 (2000).